Plasma studies of a linear magnetron operating in the range from DC to HiPIMS

André Anders, and Yuchen Yang

Citation: Journal of Applied Physics **123**, 043302 (2018);
View online: https://doi.org/10.1063/1.5017857
View Table of Contents: http://aip.scitation.org/toc/jap/123/4
Published by the American Institute of Physics

Plasma studies of a linear magnetron operating in the range from DC to HiPIMS

André Anders[a),b)] and Yuchen Yang[c)]
Lawrence Berkeley National Laboratory, 1 Cyclotron Road, Berkeley, California 94720, USA

(Received 30 November 2017; accepted 3 January 2018; published online 22 January 2018)

Plasma properties of magnetrons have been extensively studied in the past with the focus on small, research-style magnetrons with planar disk targets. In this contribution, we report on plasma diagnostics of a linear magnetron because the linear geometry is widely used in industry and, more importantly here, it provides the unique opportunity to align a linear racetrack section with a streak camera's entrance slit. This allows us to follow the evolution of plasma instabilities, i.e., localized ionization zones or spokes, as they travel along the racetrack. This report greatly extends our more limited and focused study on the structure and velocity of spokes [Anders and Yang, Appl. Phys. Lett. **111**, 064103 (2017)]. Following recent plasma potential measurements [Panjan and Anders, J. Appl. Phys. **121**, 063302 (2017)], we interpret optical emission information with localized electron heating. We confirm that for low direct current operation, spokes move in the $-\mathbf{E} \times \mathbf{B}$ direction, and in the opposite direction in the high current mode. Streak images indicate slower spoke velocities near corners compared to spoke velocities in the straight sections of the racetrack. Spoke splitting and merging are observed supporting the interpretation that spoke motion represents a phase velocity of the region of greatest ionization and is not a motion of plasma. Fast camera investigations are supplemented by measurements of the energy distribution functions of ions emitted from the straight and curved regions of the racetrack, showing notable and reproducible differences. *Published by AIP Publishing*. https://doi.org/10.1063/1.5017857

I. INTRODUCTION

Magnetron plasmas have been extensively studied since the invention of sputtering magnetrons in the 1960s[1] and 1970s.[2] Research has intensified in recent years with the introduction of high power impulse magnetron sputtering (HiPIMS), a form of "ionized sputtering" where the electrical power is applied in pulses of high power in order to ionize sputtered atoms[3,4] as well as to dissociate and ionize process gas.[5] The overarching goal is to have additional "control knobs" affecting the microstructure of films deposited. Many papers and books have been published, including reviews,[4,6,7] an overview book,[8] a book on sputtering with additional ionization,[9] a book dedicated to reactive deposition[10] (since most applications require compound films), and a recent tutorial on reactive HiPIMS.[5]

The magnetron discharge turns out to be more complicated than generally thought or acknowledged. However, already in 1978, Thornton stated that "*Electron drifts perpendicular to the magnetic field develop in the presence of a perpendicular electric field, or a density gradient. Such drifts are inherently unstable, since any departure from charge neutrality in the form of charge bunching and separation (over distances of the order of the Debye length) create electric fields which cause second-order* $\mathbf{E} \times \mathbf{B}$ *drifts that can exacerbate the perturbation*."[2] The evolution of such instabilities is at the center of the present experimental investigation. Using fast cameras, traveling ionization zones or "spokes" were first observed in HiPIMS,[11–13] and then also confirmed to be present in other sputtering systems, including those at very low discharge currents.[14] Imaging and probe data showed that spoke motion in HiPIMS is in the $\mathbf{E} \times \mathbf{B}$ direction and in the opposite direction at relatively low currents typical for direct current magnetron sputtering (dcMS). Here, as usual, $\mathbf{E}$ and $\mathbf{B}$ refer to the local electric and magnetic field vectors. Spoke direction reversal has been found in the transition region at intermediate currents.[15,16]

Most research on magnetrons in R&D laboratories is done with small magnetrons having planar disk targets, while the coating industry generally uses linear (planar or rotating cylindrical) magnetrons to economically produce coatings on large areas or large batches of parts.[17] In this contribution, we extend previously demonstrated diagnostics of magnetron plasmas with disk targets to a linear magnetron and greatly expand our preliminary report.[18] Our linear magnetron is still of relatively small size compared to those used in commercial coating plants, yet it allows us to take a step in the industrially relevant direction. Most importantly, the straight portion of the racetrack offers a unique geometric opportunity to study the evolution of plasma spokes with a streak camera. A streak camera has a linear entrance slit allowing us to image the straight section of the racetrack onto the slit. In contrast to similar studies with disk-target magnetrons, the spoke remains in the field-of-view of the camera while traveling in the straight section. Spoke velocity, substructures (if present), and related phenomena can be readily seen

[a)]Author to whom correspondence should be addressed: andre.anders@iom-leipzig.de
[b)]Now at Leibniz Institute of Surface Engineering (IOM), Permoserstr. 15, 04318 Leipzig, Germany.
[c)]Now at Institute of High Energy Physics, Chinese Academy of Sciences, Academy of Sciences, Beijing, China.

with such geometry. Additionally, we can study how spokes move when departing from or arriving at the curved section of the racetrack. While the focus of this contribution is on the unique opportunity of this imaging approach, we supplement the information with measurements of species and energies of ions coming from the straight and the curved sections of the racetrack. Several target materials of different thicknesses are used to arrive at a more comprehensive picture since the plasma properties are known to depend on the target material and magnetic field, especially when operating in the HiPIMS regime.

II. EXPERIMENTAL SETUP

The experiments make use of a linear planar magnetron (Kurt J. Lesker Comp.) with a 240 mm × 120 mm target. The target thickness can be selected using a suitable clamping frame: in this study, Al, Ti, and Cu targets of 3 mm and 6 mm thickness (1/8″ and 1/4″) were used. The magnetic field was measured using a modified programmable x-y scanner moving a Hall sensor over the target surface.

The magnetron was placed in a stainless-steel high vacuum chamber of 1 m inner diameter, cryogenically pumped to a base pressure in the low 10^{-5} Pa range. Argon was introduced at a flow rate of 100 sccm with different gate valve positions to the cryogenic pump adjusting the pumping speed in order to obtain a desired pressure, typically 0.4 Pa, as specified for each experiment. In some experiments, reactive gas (oxygen, nitrogen, and by accident also air) was added to the noble gas.

As shown in Fig. 1, the magnetron was placed for many of the experiments in the center of the chamber facing a 20 cm diameter (8″) glass window for taking images with a fast-shutter or a fast streak camera. To minimize coating of the glass, the window shutter was kept closed unless an image is taken. For some experiments, the magnetron was positioned differently, so it could be seen under an oblique angle, allowing us to see plasma spokes and flares extending in both the target plane and perpendicular to it. For some other experiments, the magnetron was placed in front of a "plasma monitor," a differentially pumped, integrated quadrupole mass

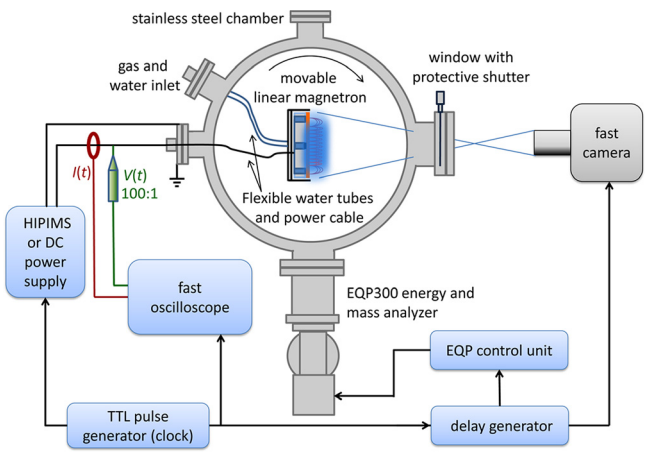

FIG. 1. Experimental setup showing the linear magnetron in a 1 m diameter vacuum chamber; the magnetron can face either the window for imaging with a fast camera or the EQP300 energy and mass analyzer.

spectrometer, and energy analyzer (model Energy Quadrupole Plasma – EQP 300 by Hiden, Ltd.), mounted on a different port on the same chamber. The flexibility of magnetron positioning allowed us to record images and ion energy distribution functions (IEDFs) in a direction normal to the target surface, but of course not at the same time.

The discharge was powered by a high current pulse generator, model SIPP2000USB (Melec GmbH), capable of delivering pulses up to 1 kV and up to 1000 A of arbitrary duration from 5 μs up to 1000 μs (or even longer for low peak power). This power supply can also serve as a dc power supply (i.e., no pulsing). In its "unipolar negative" mode, the pulser delivers negative pulses to the target, with the anode at ground. Typical pulse lengths were 20–1000 μs with repetition rates between 10 and 200 Hz. The arc control threshold was usually set to 990 A to allow for high current pulses without having the discharge terminated by the arc suppression circuit. We always recorded the target voltage and thereby made sure that the magnetron operated in the magnetron mode, not in the arc mode: arcs, if present, can be easily recognized since they have a much lower cathode-anode voltage than magnetron discharges. To monitor the voltage, a 100:1 voltage divider probe (model P5100 by Tektronix) was attached to the power feedthrough. The discharge current was recorded using a current transformer (model 101 by Pearson), when operating with pulsed discharges, and using a dc volt meter (Fluke 189) across a low-impedance shunt resistor when investigating dc magnetron sputtering (dcMS). All electrical signals were recorded with a fast 4-channel digital oscilloscope (Tektronix).

Two camera types were employed. One was a gated Intensified Charged Coupled Device (ICCD) camera (model PIMAX 4 by Princeton Instruments), equipped with an $f = 135$ mm Nikon lens. The spectral response of the PIMAX detector is from 200 to 900 nm; however, at the short wavelength range, the recording starts at a wavelength of about 300 nm limited by the optical transmission of the glass window. The PIMAX 4 is able to take single images with very short shutter (imaging) times. High image amplification has to be used for shutter speeds of less than 3 ns, leading to "noisy" (grainy) images. We typically used 3 ns imaging times to obtain snapshots of the HiPIMS plasma emission, and 500 ns for dcMS plasmas. Using various exposure times, it was tested that these times are sufficiently short to avoid blurring of the images by the motion of spokes.[12,19] When using the aluminum target, some images were taken through narrow-band spectral filters to capture the emission from selected intense spectral lines, as described in Ref. 20.

The second camera was a streak camera (model C7700 by Hamamatsu), equipped with an $f = 135$ mm Nikon lens and detector module C4742-98 whose spectral response is in the range 300–1060 nm. This camera is in the center of the current report because the slit geometry can be matched to one of the two straight sections of the racetrack. The part of the target projected onto the streak camera slit was 1 mm wide and 20 cm long and was put along the straight part of the magnetron's racetrack at a position of $y = 1.7$ cm (for the coordinate system see Figs. 2 and 3). A comprehensive set of streak and fast-shutter camera images has been acquired for

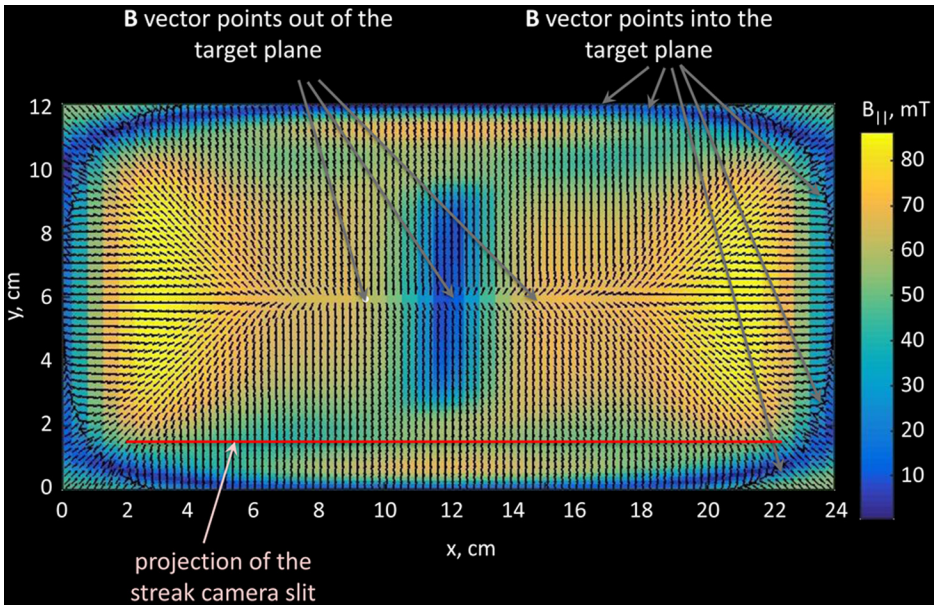

FIG. 2. The (x,y) component of the magnetic field measured in a plane $z = 1$ mm above the target surface; the strength of the field is indicated by a color while the direction by small back arrows. The entrance slit of the streak camera is projected over one of the linear sections of the racetrack, at $y = 1.7$ cm, as indicated.

magnetron plasmas operating at various currents and pressures. All images are presented using the false color scale "royal" of the image processing software IMAGEJ.[21] Additionally, following our preliminary work with a round Al target,[20] we used the same narrow-band spectral filters that allowed us to record images in the light of selected Al I and II, as well as Ar I and II spectral lines. The emitted intensity for each line carries information on the population of the upper level of the emitting ions and atoms. The upper energy level is populated by collisions of atoms and ions

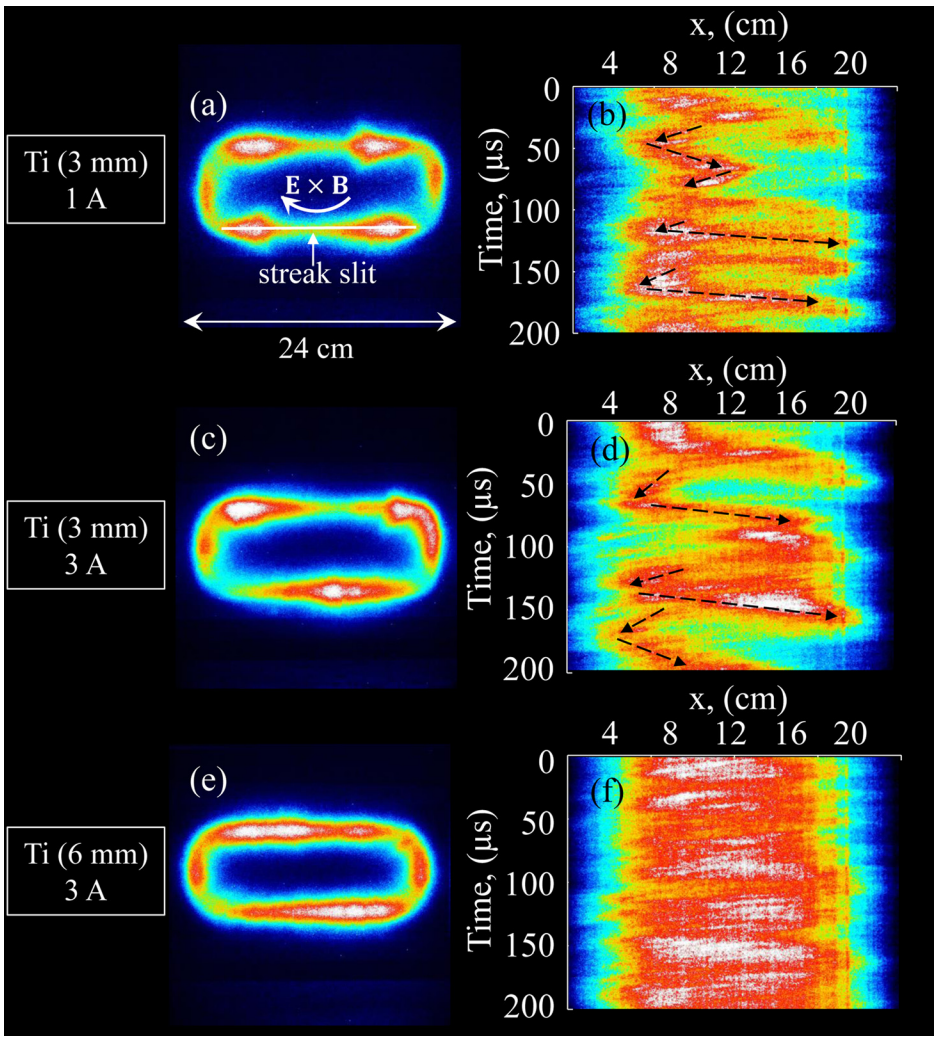

FIG. 3. Fast shutter images (left) and streak images (right) for dcMS discharges using Ti targets of different thickness and discharge current, as indicated. The false color indicates light intensity integrated of the visible spectral range, with white most intense and blue low intensity. The streak camera's slit projection is indicated in subfigure (a). Arrows in subfigures (b) and (d) point out that spokes can propagate in different directions. The slope in a streak image directly shows propagation direction and velocity. No spokes are visible at the ends of the slit because they moved outside the narrow observation region defined by the slit projection.

with electrons that have at least the energy of the upper level in question. This means that spectrally resolved images carry information on the spatial distribution of electron energy.[20]

The setup for measuring ion energy distribution functions (IEDFs) is similar to our previous work,[22] using the EQP300 with an entrance orifice of 100 μm diameter. Using the narrow acceptance angle of the instrument, which is discussed in Sec. IV, IEDFs were measured for ions coming from the corner region ($x = 3$ cm and $y = 10$ cm) and from straight region of the racetrack ($x = 12$ cm and $y = 10$ cm). The distance between target and EQP entrance orifice was 250 mm. IEDFs were recorded in voltage steps of 0.5 V up to a potential of 100 V (corresponding to 100 eV for single charged ions, 200 eV for doubly charged ions, etc.). The detector dwell time (the time over which signals were accumulated) was 2000 ms for each energy and mass data point, which means that we effectively integrated each measurement over this time, or averaged over many pulses in the case of pulsed discharges. Strictly speaking, the instrument does not measure mass and energy but mass/charge and energy/charge. Therefore the usual binning procedure was applied, namely, multiplying the raw data by the charge state and dividing the count number by the applicable charge state number.

III. RESULTS

A. Magnetic field

The magnetic field of the magnetron is shown in Fig. 2. More precisely, this is the field component parallel to the target as measured in the plane 1 mm from the surface of a 3 mm thick target surface. One can see that the magnetic field is slightly non-uniform and very slightly asymmetric: the point where the measured **B**-field has only a z-component is approximately 3 mm off the center line of the magnetron. This could be a magnetron issue or a systematic error of the probe positioning, or a combination of both. The magnetic field along the straight section of the racetrack has at least $\pm 10\%$ deviations from the average, which may play a role in forming "primordial" spokes from uniform plasma, which are then amplified as pointed out by Thornton (see Sec. I).

B. Imaging results for DC magnetron sputtering

A selection of fast-shutter and streak images taken in dcMS mode is shown in Fig. 3. By comparing fast-shutter images 3(a) and (c), it can be seen that higher currents lead to less spokes. As evident by the slop of the patterns in streak images, subfigures (b) and (d) show that spokes generally travel in the $-\mathbf{E} \times \mathbf{B}$ direction, and the spoke velocity is higher at higher current. However, spokes usually slow down and may even change the direction when approaching the corner. For the 6 mm thick Ti target, the magnetic field at the target surface is approximately 20 mT lower than for the 3 mm thick target; the spokes are more elongated along the racetrack, and their number is smaller. The spokes are irregular and appear even chaotic at times.

At higher time resolution (Fig. 4), obtained by a shorter camera sweep time of 100 μs or less, one can clearly discern

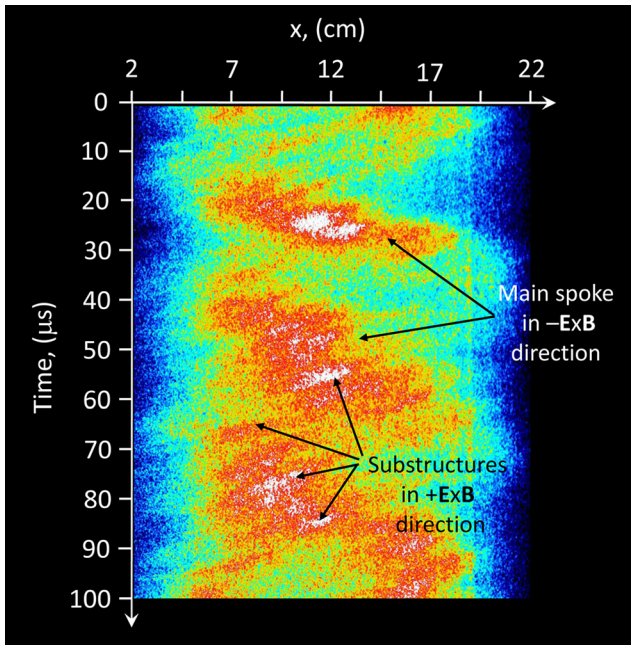

FIG. 4. Streak image with the straight section projected as in Figs. 2 and 3, here 100 μs sweep time, dcMS with Ti target, 1 A, 250 V, Ar 0.4 Pa: while the main spoke usually travels from left to right ($-\mathbf{E} \times \mathbf{B}$ direction), the substructures appear with the opposite slope, indicating propagation in the $+\mathbf{E} \times \mathbf{B}$ direction.

that the spokes in dcMS have substructures that travel in the opposite, the $\mathbf{E} \times \mathbf{B}$ direction, which is the direction of the electron drift.

C. Imaging results for HiPIMS

Comparing HiPIMS with dcMS with images, it is apparent that the plasma spokes look and behave differently. Figure 5 shows different fast-shutter images taken at different times into the rising HiPIMS current pulse. The 6 mm thick Ti target has a weaker magnetic field than the 3 mm thick Ti target and therefore needs higher voltage to reach the same current (thus comparing images at the same current implies considering different power levels). The spokes of the 3 mm thick Al target are much more localized than spokes on other targets. For the 3 mm thick Cu target, there is a transition from spokes to a spoke-free mode at high current. Related streak images are shown in Fig. 6 with conditions as indicated in subfigures.

Images in Figs. 6(a) to 6(d) were taken at currents of about 400 A in the middle of the pulses. As one can see, the spoke behavior is more complicated in HiPIMS than in dcMS, requiring us to take many more images to better comprehend the situation. From the more than 50 images taken for each current-pressure-target combination, for the Ti and Al targets of 3 mm thickness, we could derive that most spokes speed up when approaching the center section of the linear racetrack and slow down when approaching the corner. However, for the 6 mm thick Ti target and the 3 mm thick Cu target, most spokes propagate at approximately constant velocity. Images 6(e) to 6(h) were taken at a current of about 900 A near the end of the pulses. For the 6 mm thick

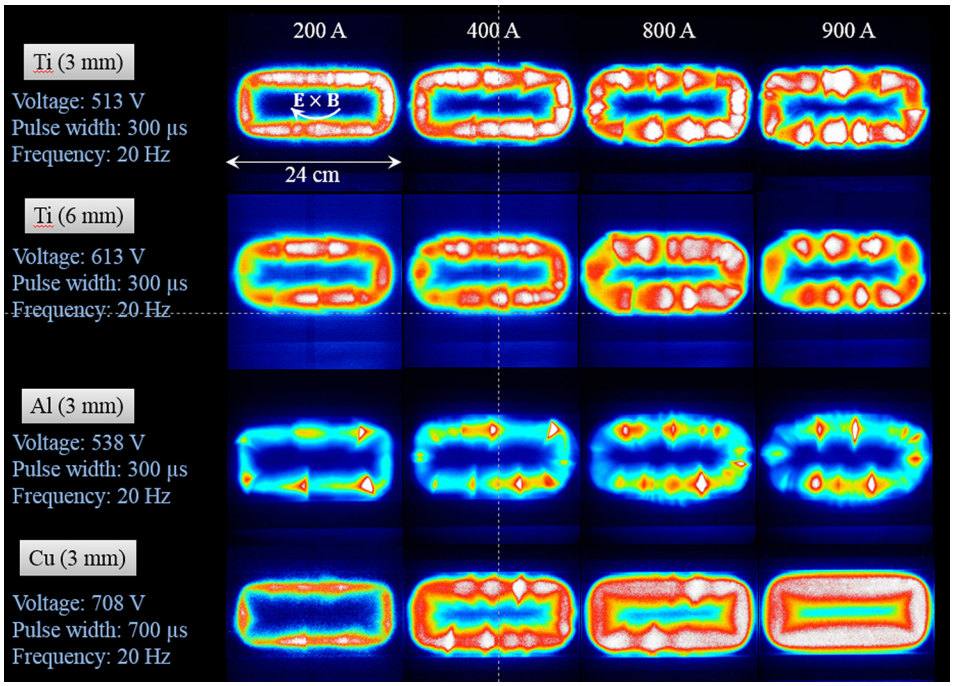

FIG. 5. Fast (3 ns) shutter images of HiPIMS discharges in false color representation of the light intensity integrated over the visible spectral range. Four different targets have been used: 3 mm thick Ti, Al, and Cu targets and a 6 mm thick Ti target, with the discharge conditions as specified in each subfigure. Images were taken at different times into the rising current pulse; hence the snapshots are for different currents but for the same applied voltage.

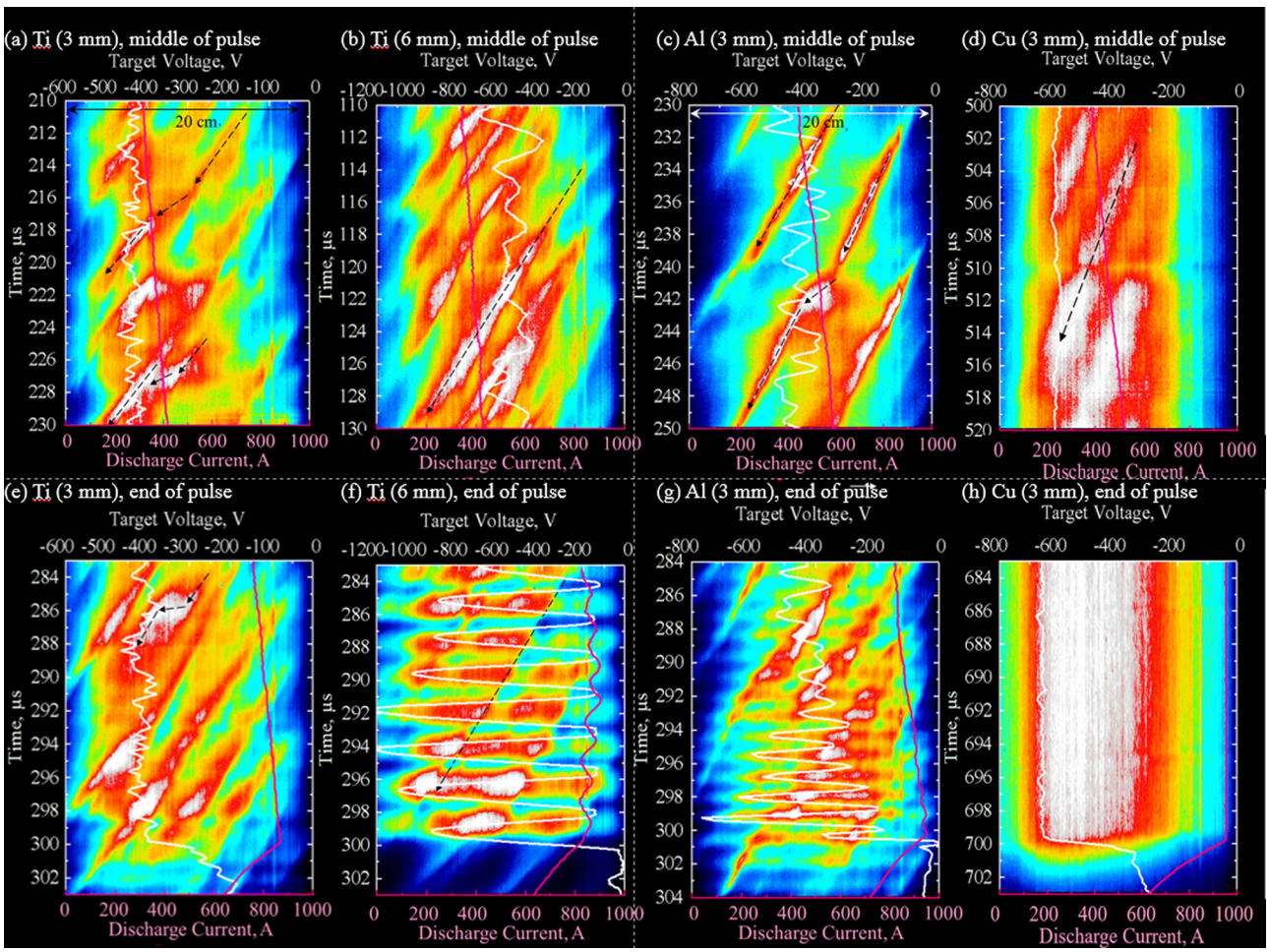

FIG. 6. Very busy composite images of HiPIMS discharges comprised of streak images, with spatial length of 20 cm and sweep time of 20 μs, overlaid with voltage and current curves; (a) for a 3 mm thick Ti target, (b) for a 6 mm thick Ti target, (c) for a 3 mm thick Al target, and (d) for a 3 mm thick Cu target taken in the middle of the pulse; and with (e) for a 3 mm thick Ti target, (f) for a 6 mm thick Ti target, (g) for a 3 mm thick Al target, and (h) for a 3 mm thick Cu target, taken at the end of the discharge pulse. All discharges were of 300 μs pulse length at a pulse repetition rate of 20 Hz.

Ti target and the 3 mm thick Al target, the HiPIMS target voltage and power exhibit strong oscillations, leading to corresponding oscillations of light emitted by the plasma.

In the following, we elaborate on a few situations which may help to elucidate the underlying physics. First, we consider copper-HiPIMS. It is well known that the plasma composition greatly depends on the self-sputter yield of the target material. Copper is the most-researched target material of high sputter yield: the HiPIMS-plasma is dominated by metal and under certain conditions one can even run the discharge in vacuum, without any process gas.[23] For convenience of starting the discharge, gas is usually introduced. Figure 7 shows that early in the copper HiPIMS-pulse, spokes appear in a pronounced way but rather chaotic, while later in the pulse, at higher currents, spokes affect each other such as to produce regular, self-organized patterns (Fig. 7).

When the copper HiPIMS pulse progresses with discharge current exceeding about 400 A, the spokes merge and the plasma becomes azimuthally uniform; this has been reported before.[19] Now, using the streak camera with a linear magnetron, the transition can be directly observed (Fig. 8).

Switching to examples of reactive HiPIMS with a titanium target in Ar-N_2, we do not find the transition to a spoke-less mode, at least not for the current range under investigation (<1 kA). As illustrated in Fig. 9, one recognizes regular patterns of spokes though their speeds, as readily evident by their slopes in streak images, are not exactly the same. When a faster spoke approaches its predecessor, energetic electrons seem to "catch up" and the spokes merge. In other occasions, spokes split up. Later in the pulse, oscillations appear that let all spokes simultaneously become periodically dimmer or brighter.

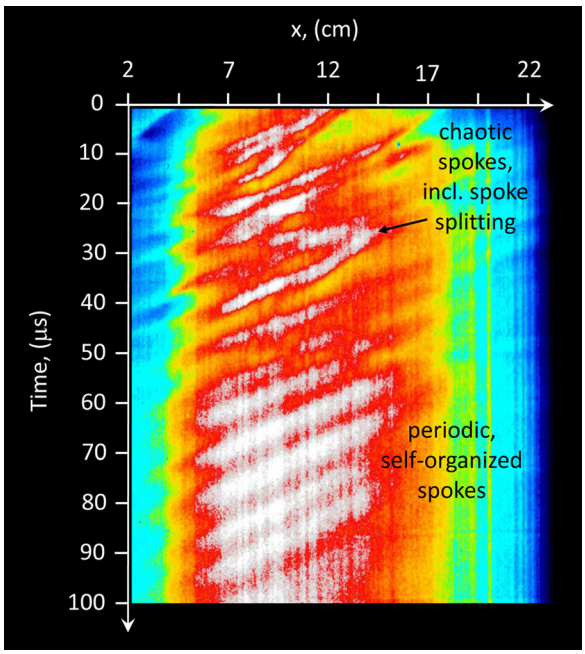

FIG. 7. Streak image of a straight section of the linear magnetron, 100 μs streak in the middle of the 300 μs, and Cu-HiPIMS pulse with a peak current of 700 A.

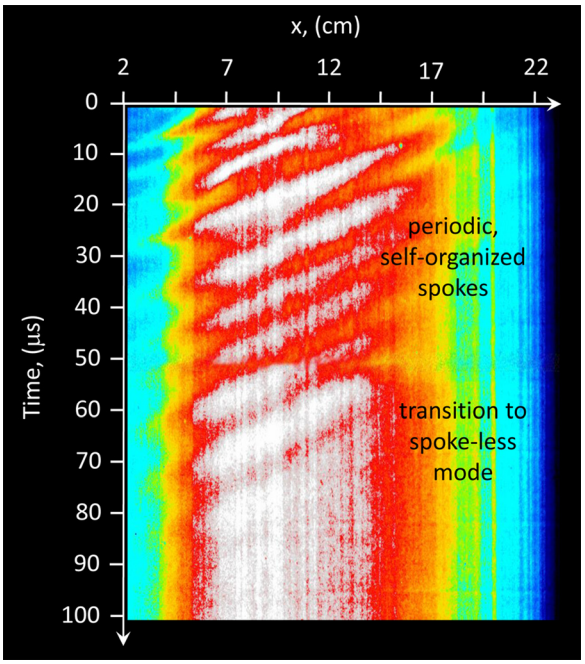

FIG. 8. Streak image of 100 μs duration near the end of a 300 μs Cu-HiPIMS pulse leading to a peak current of 700 A: one can clearly see the transition from a periodic, self-organized spoke mode to a spoke-less mode. Although this is a different pulse than the one shown in Fig. 7, one can visualize that Fig. 8 is like a continuation of Fig. 7.

D. Spectrally resolved images

In order to use the spectral information in the light emitted by the plasma, spokes have been recorded with selected spectral filters allowing us to see the spokes in light of specific optical transitions of metal or gas ions and atoms. Aluminum is particularly suited for such study because its atom and ion lines are grouped and separated so that the use of narrow-band spectral filters is easily applicable. Figure 10 shows the result, with the lines and other parameters specified in the figure and figure caption.

E. Oblique angle imaging in dcMS

Viewing the magnetron under an oblique angle allows us to visualize the plasma distribution not only along the racetrack but also in the z-direction. This allows us to observe plasma flares should they be present. One can see spokes, and some of them have a rather sharp edge (Fig. 11).

F. Oblique angle imaging in HiPIMS, including spectrally resolved images

Further interesting images can be obtained when viewing the linear magnetron under oblique angle view in HiPIMS-mode: features like spoke groupings and flares are clearly visible. As with the straight-on view (Fig. 10), images showing the light of different spectral lines were taken at different times (different HiPIMS pulses), and therefore, each shows a somewhat different plasma structure. Note that the apparent intensity of images using different spectral lines should not be compared as various factors play a role such as the spectral sensitivity of the detector and the camera's image intensification setting, the latter being adjusted for

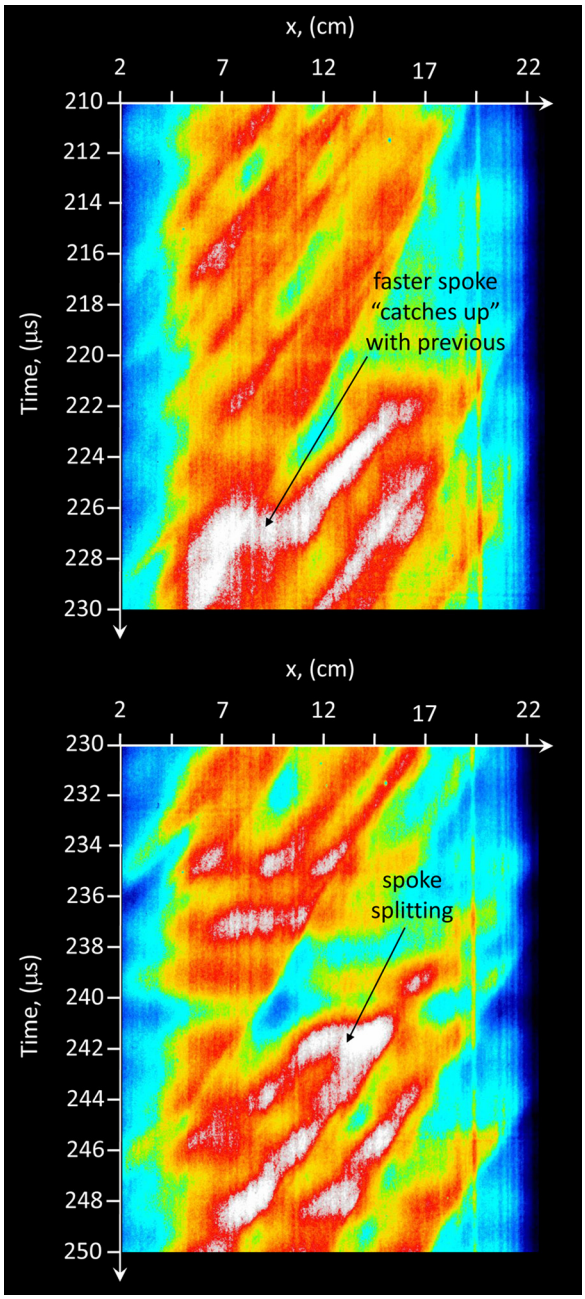

FIG. 9. Two streak images (of different pulses) of 20 μs duration for reactive HiPIMS of a 6 mm thick Ti target in 0.43 Pa Ar and 16 mPa N_2 near the middle (top image) and end (bottom image) of the pulse; 613 V applied voltage of a 300 μs HiPIMS pulse leading to a peak current of 900 A. One can see features like spoke splitting and merging.

each spectral line to make best use of the dynamic range of the detector.

G. Ion energy distribution functions (IEDFs)

To supplement the information that can be gained from fast camera imaging, we further investigated the differences between the plasma ion flow originating at the corner and from the linear racetrack section by measuring the IEDFs with the instrument aligned with the corner at $x = 3$ cm and $y = 10$ cm (black curves in Figs. 13 and 14), and with the center of the linear racetrack at $x = 12$ cm and $y = 10$ cm (red curves in Figs. 13 and 14). Figure 13 shows the results for the 3 mm thick Ti target in argon, and Fig. 14 the corresponding results with 6 mm thick target, i.e., where the magnetic field above the surface is weaker.

IV. DISCUSSION

Optical emission spectroscopy of magnetron plasmas shows that the light is primarily composed of many spectral lines of atoms and ions while the contribution of continuum radiation is small (many papers, for example, Refs. 24 and 25). Therefore, when we interpret frame and streak images, we should keep in mind that the observed light is emitted from excited species (atoms, ions), where most of the upper levels of the optical transitions are populated by collisions of ground state atoms or ions with energetic electrons (electrons having a kinetic energy of at least the excitation energy). Given that de-excitation occurs relatively quickly after excitation, the gated images show us the 2D spatial distribution of the excitation rate, while streak images show the 1D-spatial and time distributions. To better understand what we are seeing, we need to discuss the excitation rate from the ground state "0" to an upper level "u," $dn_{0\to u}/dt$, which depends on the density of ground state atoms n_0 (or ions, if light from ions is considered) and electrons energetic enough to cause excitation, i.e., the electron density n_e times a convolution integral involving the excitation cross section $\sigma_{0\to u}(E)$ and electron energy distribution function, $f_e(E)$, thus

$$\frac{dn_{0\to u}}{dt} = n_0 n_e \int f_e(E)\, E^{1/2}\, \sigma_{0\to u}(E)\, dE. \tag{1}$$

In our images, we record light integrated over all or a portion of the visible spectral range, from a lower limit $\lambda_{\min}$ to a maximum $\lambda_{\max}$. The recorded intensity can be described by the sum of all optical emissions in this range, i.e., optical transitions from upper levels u to lower levels l, where the intensity of the individual line depends on its Einstein coefficient A_{ul} and is proportional to the density of atoms excited in the upper level n_u

$$I_{ul} = K\, A_{ul} n_u E_{ul}, \tag{2}$$

where K is a geometry factor, and $E_{ul} = h\nu_{ul} = hc/\lambda_{ul}$ is the energy of the optical transition, with h and c having the usual meaning of Planck's constant and the speed of light in vacuum. The recorded intensity is also affected by the transmittance of the optical elements, like windows and lenses, and by the spectral sensitivity of the detector. Those features can be collectively expressed by a spectral factor $S(\lambda)$, and the intensity shown in our images is therefore

$$I = K \sum_{\lambda_{\min}}^{\lambda_{\max}} S(\lambda) A_{ul} n_u E_{ul}. \tag{3}$$

When we used spectral filters, like in Figs. 10 and 12, the spectral range was narrow and dominated by one spectral line whose wavelength λ_{ul} and upper energy level was indicated. From Eq. (3), one can see that the key factor is the density of species in the upper level, which is determined by

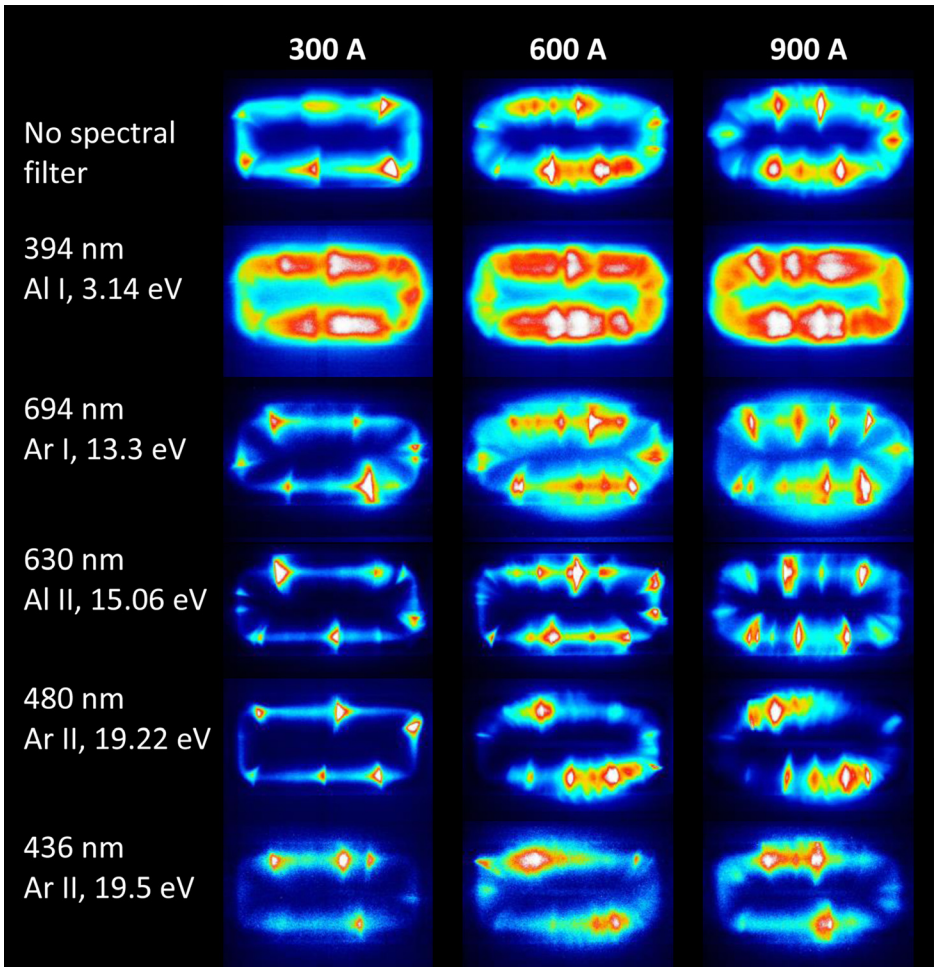

FIG. 10. Spectrally resolved images, with exposure time of 50 ns, of the linear magnetron with an Al target, 0.3 Pa Ar, 250 μs HiPIMS pulses, at 50 Hz repetition frequency, with peak current of 900 A at the end of each pulse. The left column shows the optical wavelength recorded, the emitting atom or ion species, and the upper energy level of the optical transition. The intensity of the images is affected by the image amplification settings, which was optimized for each spectral line given the dynamic range of the detector. Therefore, no conclusion should be drawn based on comparison of displayed intensities of different spectral lines.

the balance of excitation, Eq. (1), and de-excitation, which can be collisional or radiative.

In the case of dcMS, the density of ground state atoms is relatively evenly distributed since the neutrals of the process gas (like argon atoms or nitrogen molecules) dominate the particle density at all times. Apart from rarefaction (a density reduction) near the target,[26] caused by the "sputter wind" from the target and by target heating, the process gas density is practically equal everywhere and is much larger than the density of sputtered atoms. Therefore, keeping Eq. (1) in mind, *images in dcMS represent the excitation conditions* given by the density of electrons and their energy distribution function.

The appearance of spokes and other patterns indicates that the excitation (and ionization) conditions are not uniformly distributed, or, in other words, that electrons have different energies depending on their location and conditions affecting the energy distribution function. Energizing electrons in the magnetron's presheath, where the plasma is quasi-neutral yet a notable voltage drop can be present, has been explained in an ionization region model by Huo *et al.*[27] While ionization region models[28–31] are still limited to electron energization uniformly distributed along the racetrack, it was pointed out[32] that sheath energization is localized, giving rise to spokes and related structures. It was deduced that the potential structure necessary to give electron energy involves a transition from low to high potential, i.e., a potential hump should exist at locations where electrons are energetic and the plasma is bright.[33] This has recently been confirmed by plasma potential measurements.[34]

Images like those shown in Figs. 3 and 4 show spokes moving in the $-\mathbf{E}\times\mathbf{B}$ direction with a fine substructure moving with higher velocity in the opposite direction. As was mentioned in our preliminary report,[18] the $-\mathbf{E}\times\mathbf{B}$ direction for a spoke is the "natural" direction one should expect since electrons, drifting in the $\mathbf{E}\times\mathbf{B}$ direction, arriving at a spoke on its $-\mathbf{E}\times\mathbf{B}$ side, where most ionization occurs. Ions are accelerated by the local electric field in the general $-\mathbf{E}\times\mathbf{B}$ and in the target directions, which leads to a displacement of the space-charge double layer in the general $-\mathbf{E}\times\mathbf{B}$ direction.[34] From images like the one shown in Fig. 4, we can deduce that the electrons responsible for excitation and ionization are not flowing uniformly but appear pulsating in little bursts or bunches, causing a substructure to appear that coincides with the drift direction of electrons. From the slope of the structures in streak images (Fig. 4), we can readily find a velocity of about 5000 m/s for the spoke motion (main structure) and slightly more than 10^4 m/s for the substructures. Assuming that the main contribution to electron drift comes from the $\mathbf{E}\times\mathbf{B}$ drift, associated with a velocity $|\mathbf{v}_{\mathbf{E}\times\mathbf{B}}| = E/B$, and magnetic field is of order 0.1 T, the electric field should be in the range 10^3 V/m, or 10 V/cm, which is the right order of magnitude in the magnetic presheath according to potential measurements.[34] One can also

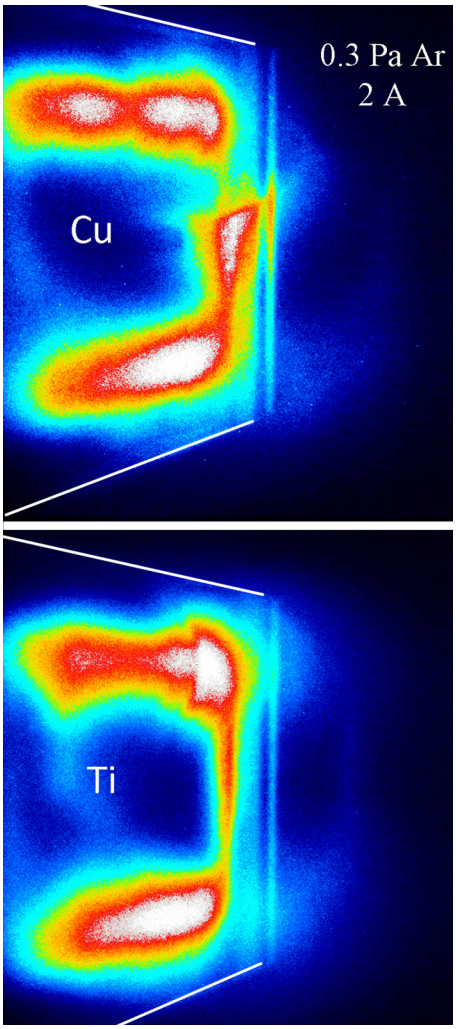

FIG. 11. Oblique angle view at one end of the linear magnetron, operating in dcMS, in argon of 0.3 Pa, current 2 A, 500 ns camera gate time; top: Cu target, bottom: titanium target. White lines added to better show the outline of the target; the vertical line in the middle of each picture is a reflection from the anode frame surrounding the target.

look at this finding differently, namely, that the assumption that the substructures are related to the electrons' $\mathbf{E} \times \mathbf{B}$ drift is reasonable.

The frame images of HiPIMS discharges (Fig. 5) show a great target-dependence of the light emitted, evidence that the plasma is determined by the target metal. There is a remarkable difference of the width and "sharpness" of the spokes, which should be interpreted by considering the upper energy levels of the spectral lines contributing to the images. The lower these levels, the more electrons can participate in the excitation process, and the spokes appear broader and blurred. This is directly illustrated by using spectral resolution as done in Fig. 10, where images are taken through spectral filters. One can see that spokes tend to be more pronounced and distinctly brighter than their surroundings when observed in the light coming from the more energetic upper levels of the optical transition. Therefore, the images of Fig. 10 suggest that the interpretation via localized electron heating, originally introduced in the context of small round magnetrons operating in HiPIMS mode,[20] is also fully applicable to linear magnetrons. The conclusion should be

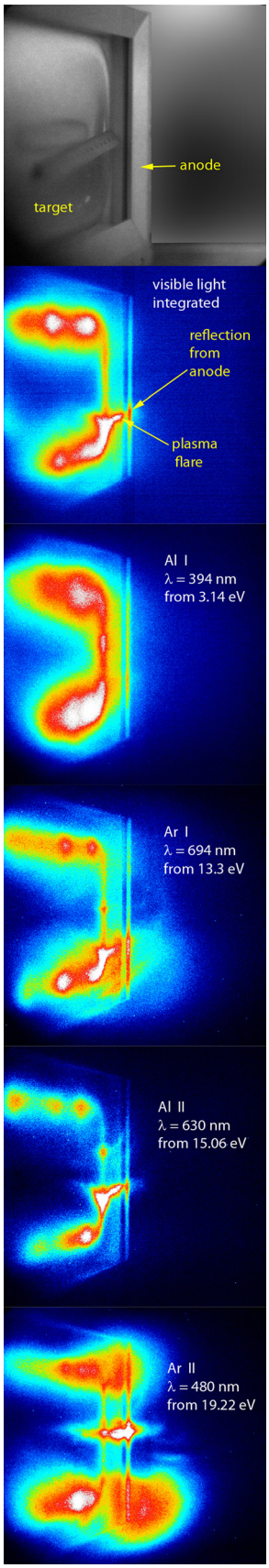

FIG. 12. Oblique angle observation of plasma of different HiPIMS pulses, Al target in 0.3 Pa argon, 590 V applied voltage, 800 A peak current at the end of 240 μs pulses, with the light spectrally integrated or resolved, as indicated in each subfigure. The top subfigure is an image of the magnetron in ambient light, and images below are in light as indicated by the labels, where the energy (in eV) refers to the upper level of the optical transition.

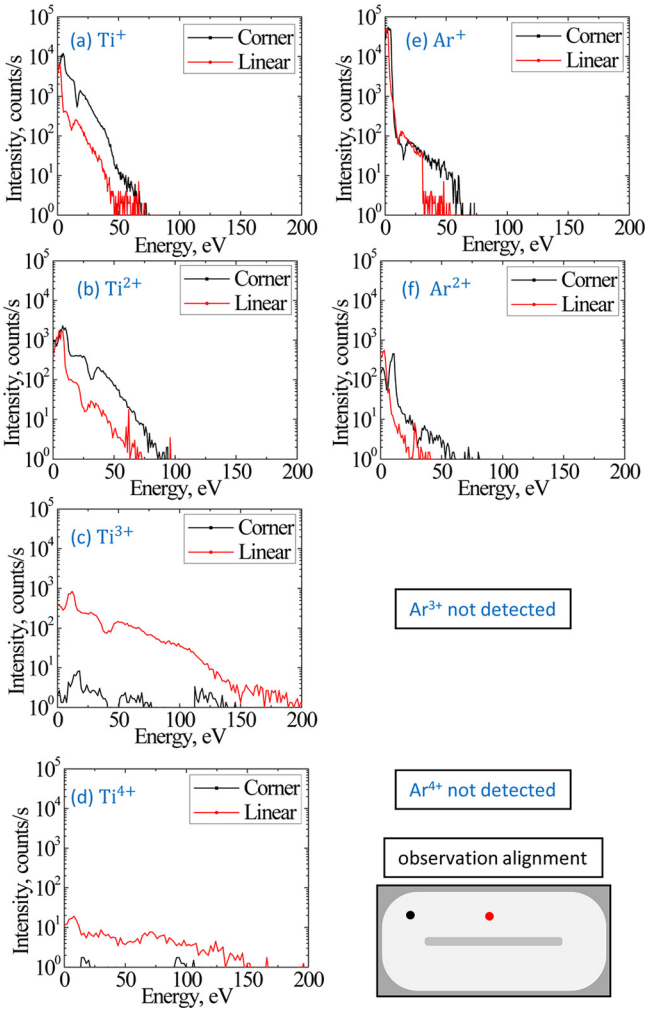

FIG. 13. IEDFs measured for a 3 mm thick Ti target operated in 0.4 Pa argon, 513 V, 800 A peak current, 10 Hz, 400 μs pulse on time, each distribution is averaged over 20 pulses. The alignment of the entrance orifice relative to the target is indicated by the dots in the sub-image placed in the lower right corner of the figure.

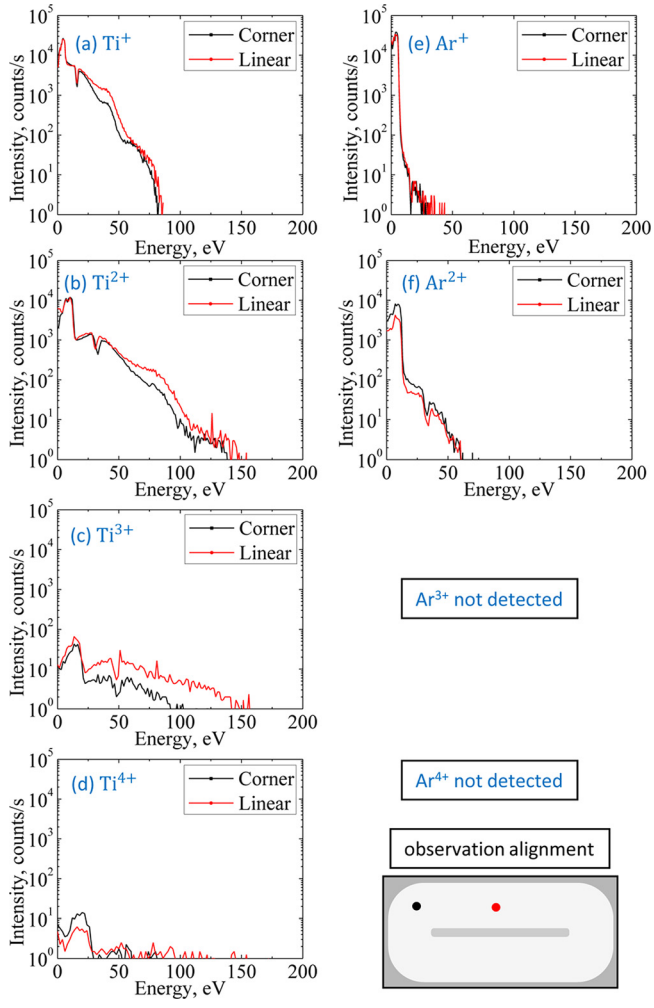

FIG. 14. Similar to Fig. 13 but with a 6 mm thick Ti target; the voltage was adjusted to 544 V in order to arrive at the same peak current of 800 A, all other parameters like in Fig. 13.

considered when interpreting the light from other targets where the spectral line separation is not as easily done because various atom and ion lines are closer than the spectral width of available spectral filters.

Figures 6–9 show that the great variation spokes have under different conditions, with evidence for turbulence but also self-organization. The latter requires that one spoke influences the other. For example, as argued earlier,[35] a spoke produces locally enhanced sputtering and the time needed for the sputtered atoms to reach a certain distance ($\sim$1 mm) from the target may or may not coincide with the arrival of the following spoke. For suitable timing, the arriving spoke "finds" plenty of neutrals to be ionized, the density factor in Eq. (1), and the ionization rate can be high. It is also conceivable that the timing of supply is not right, and in this case, weakening the following spoke. As we see, for example, in Fig. 7, even within one HiPIMS pulse, the conditions can change leading from a chaotic to regular pattern.

The disappearance of spokes for the high-yield material copper (Fig. 8) can be interpreted using a very general instability argument: Spokes are typical for most $\mathbf{E} \times \mathbf{B}$ discharge conditions since they facilitate "anomalous" electron transport across magnetic field lines to the anode.[12,36,37] They help that the discharge can exist since collisions alone may be insufficient to provide charged particle transport. However, given the very high sputter yield of copper, the supply of copper atoms can be so large that collision-based cross-**B**-field transport is sufficient, and hence the need for spokes disappears. Future transport simulations will be needed to test this interpretation.

Merging and splitting of spokes, as seen in Fig. 9, are other interesting observations. We see that spokes can have different slopes in streak images, which means the cause for their displacement has different strengths. We deduce that the electric double layer at the spoke edge may have an electric field component parallel to the target that is not the same for all spokes. When one spoke approaches its predecessor, it eventually catches up and merges in a rather abrupt process, as shown in Fig. 9, top image. One could speculate that the electron drift speed suddenly increased; however, we should keep in mind that spoke motion is indicative for a phase velocity, the displacement of a location of enhanced excitation and ionization, and not a group velocity showing transport of ions or electrons. Therefore, it is possible that the

apparent jump of one spoke to the predecessor is horizontal in the streak images, indicating "infinite" velocity within our velocity resolution. Also, the splitting of spokes, as shown in the bottom image of Fig. 9, is a splitting of excitation and ionization conditions associated with a restructuring of electron heating conditions, i.e., the potential structure, and not necessarily a splitting in terms of particle motion.

Oblique angle view images like Fig. 11 underpin previous interpretations and add that most of the ionization occurs very close (∼1 mm) to the target. The spectrally resolved images of Fig. 12 give even deeper insight, namely, that the excitation and ionization of metal atoms occurs closer to the target than the excitation and ionization of argon.

The last information may be useful information when interpreting the ion energy distribution functions (IEDFs) shown in Figs. 13 and 14. There are surprisingly reproducible differences in IEDF for the various ion species for which further studies are needed, and especially suitable simulations could help to interpret the results. Here we just highlight some findings and offer thoughts related to those mechanisms.

The IEDFs typically show a peak at low (thermal) energy and a tail reaching high energies, especially under HiPIMS conditions, in agreement with earlier reports in the literature.[22,38–42] Notably, we detect multiply charged target ions Ti^{3+} and Ti^{4+}, proof for the presence of very energetic electrons. The extent of the energetic tail of the distributions for metal ions was found approximately proportional to their charges, indicative for an electric field mechanism presuming that those ions were generated at about the same location. Spectrally resolved images suggest that Ar^{2+} ions are generated at locations slightly further away from the target than Ar^{+} ions.

In any case, the peak of the IEDF is at low (thermal) energy of just a few eV, which is consistent with probe measurements that the potential humps of spokes are essentially near ground, i.e., the absence of high absolute positive potential in potential humps. High energy ions are much less frequent, and their energy gain must come from an acceleration in varying electric fields, such as those arising from the breathing instability[43] and/or energy gained by the electric field component parallel to the target,[33] both mechanisms in concert with collisions which establish the tail of distribution. A related observation is that the shape of the IEDFs depends on the charge state: the IEDF of higher charged ions exhibits energy tails with a slow fall-off, extending much further to high energy.

There are significant differences in the IEDFs for ions coming from different regions of the racetrack of a linear magnetron, which were hitherto not reported. Here, we make use of the fact that energy analyzers such as the EQP300 have a narrow acceptance angle of a few degrees, i.e., ions are only detected and counted if they enter the instrument's entrance orifice within a few degrees to the normal of the entrance plane.[44] The specific acceptance angle slightly depends on the ion species and their energy, and is largest for ions of very low energy. Ions scattered on their way to the EQP's entrance may have changed direction and are thus not detected, which implies that most of the detected ions are those arriving with no or very few collisions. Using the directionality of the detection one can clearly see that metal ions coming from a straight section of the magnetron have higher charge states and energies than ions coming from the corner region. This is not the case for argon ions, also indicative that the main ion production regions are different for target ions versus background gas ions.

The above comments refer to observations shown in Fig. 13. Looking at Fig. 14, where the same target material was used but the magnetic field was weaker due to the greater target thickness, the IEDFs are similar though the differences in terms of ions coming from the corner versus straight section are much smaller. Remarkably, distribution features like the slope and in some cases local maxima and minima are reproducible. Again, further simulations are needed to better understand these features.

V. CONCLUSIONS

Summarizing, using a linear magnetron provided a unique opportunity to study plasma features of a magnetron because spokes stay in the field of view of a streak camera when moving along the racetrack. With high spatial and temporal resolution and without averaging, streak images show spoke evolution for a variety of conditions, from dcMS to HiPIMS, their interaction including merging and splitting, and the presence of substructures. The findings confirm and complement many of recent publications where spokes were found to be present under most of a magnetron's operation conditions. In fact, with the exception of high power sputtering of high-yield materials like copper, where collisions are sufficient to facilitate particle transport across magnetic field lines, spokes seem to be omnipresent, fulfilling an important function in facilitating "anomalous" transport of charge. In that sense, the ionization instability actually stabilizes the magnetron discharge. Spokes are described as locations of enhanced excitation and ionization, and therefore their motion relative to the target should not be set equal to motion of charged particles. This understanding resolves the issue why spokes can merge or split with what sometimes appears as "infinite" velocity.

The here-presented streak camera study is complemented by frame images, including spectrally resolved images in end-on and oblique angle view, and by measurements of energy distribution functions of ions emitted from a straight section versus the corner region of a linear magnetron. Those complementary results help to get a relatively comprehensive picture of the magnetron discharge plasma; however, it is also clear that many of the observed features still lack a quantitative description by modeling and simulation. Our experimental results suggest that the ionization region model, where electrons are energized in the magnetic presheath, seems to be poised to explain much of the observation provided electron heating is described not only globally but also locally, namely, associated with the electric field of spokes.

ACKNOWLEDGMENTS

We thank Joe Wallig for help setting up the system and Shuo Xu and Sebastien Tetaud for assistance in some of the

measurements. The Kurt J. Lesker Company kindly provided the linear magnetron. This work was done at Lawrence Berkeley National Laboratory with support by the U.S. Department of Energy, under Contract No. DE-AC02-05CH11231.

[1]E. Kay, "Magnetic field effects on an abnormal truncated glow discharge and their relation to sputtered thin-film growth," J. Appl. Phys. **34**, 760 (1963).
[2]J. A. Thornton, "Magnetron sputtering: Basic physics and application to cylindrical magnetrons," J. Vac. Sci. Technol. **15**, 171 (1978).
[3]V. Kouznetsov, K. Macak, J. M. Schneider, U. Helmersson, and I. Petrov, "A novel pulsed magnetron sputter technique utilizing very high target power densities," Surf. Coat. Technol. **122**, 290 (1999).
[4]J. T. Gudmundsson, N. Brenning, D. Lundin, and U. Helmersson, "High power impulse magnetron sputtering discharge," J. Vac. Sci. Technol. A **30**, 030801 (2012).
[5]A. Anders, "Tutorial: Reactive high power impulse magnetron sputtering (R-HiPIMS)," J. Appl. Phys. **121**, 171101 (2017).
[6]U. Helmersson, M. Lattemann, J. Bohlmark, A. P. Ehiasarian, and J. T. Gudmundsson, "Ionized physical vapor deposition (IPVD): A review of technology and applications," Thin Solid Films **513**, 1 (2006).
[7]P. J. Kelly and R. D. Arnell, "Magnetron sputtering: A review of recent developments and applications," Vacuum **56**, 159 (2000).
[8]*Handbook of Deposition Technologies for Films and Coatings*, edited by P. Martin (William Andrew/Elsevier Science, Norwich, NY, 2009).
[9]*Ionized Physical Vapor Deposition*, edited by J. A. Hopwood (Academic Press, San Diego, CA, 2000).
[10]*Reactive Sputter Deposition*, edited by D. Depla and S. Mahieu (Springer, Heidelberg, 2008).
[11]A. Kozyrev, N. Sochugov, K. Oskomov, A. Zakharov, and A. Odivanova, "Optical studies of plasma inhomogeneities in a high-current pulsed magnetron discharge," Plasma Phys. Rep. **37**, 621 (2011).
[12]A. Anders, P. Ni, and A. Rauch, "Drifting localization of ionization runaway: Unraveling the nature of anomalous transport in high power impulse magnetron sputtering," J. Appl. Phys. **111**, 053304 (2012).
[13]A. P. Ehiasarian, A. Hecimovic, T. de los Arcos, R. New, V. Schulz-von der Gathen, M. Böke, and J. Winter, "High power impulse magnetron sputtering discharges: Instabilities and plasma self-organization," Appl. Phys. Lett. **100**, 114101 (2012).
[14]A. Anders, P. Ni, and J. Andersson, "Drifting ionization zone in sputtering magnetron discharges at very low currents," IEEE Trans. Plasma Sci. **42**, 2578 (2014).
[15]Y. Yang, J. Liu, L. Liu, and A. Anders, "Propagation direction reversal of ionization zones in the transition between high and low current magnetron sputtering," Appl. Phys. Lett. **105**, 254101 (2014).
[16]A. Hecimovic, C. Maszl, V. Schulz-von der Gathen, M. Böke, and A. von Keudell, "Spoke rotation reversal in magnetron discharges of aluminium, chromium and titanium," Plasma Sources Sci. Technol. **25**, 035001 (2016).
[17]G. Bräuer, B. Szyszka, M. Vergöhl, and R. Bandorf, "Magnetron sputtering - Milestones of 30 years," Vacuum **84**, 1354 (2010).
[18]A. Anders and Y. Yang, "Direct observation of spoke evolution in magnetron sputtering," Appl. Phys. Lett. **111**, 064103 (2017).
[19]J. Andersson, P. Ni, and A. Anders, "Smoothing of discharge inhomogeneities at high currents in gasless high power impulse magnetron sputtering," IEEE Trans. Plasma Sci. **42**, 2856 (2014).
[20]J. Andersson, P. Ni, and A. Anders, "Spectroscopic imaging of self-organization in high power impulse magnetron sputtering plasmas," Appl. Phys. Lett. **103**, 054104 (2013).
[21]W. Rasband, see http://imagej.nih.gov/ij for ImageJ 1.44p (National Institute of Health, 2011).
[22]M. Panjan, R. Franz, and A. Anders, "Azimuthally asymmetric particle fluxes in sputtering magnetrons, and their amplification by ionization zones in high power impulse magnetron sputtering," Plasma Sources Sci. Technol. **23**, 025007 (2014).
[23]J. Andersson and A. Anders, "Gasless sputtering: Opportunities for ultra-clean metallization, coatings in space, and propulsion," Appl. Phys. Lett. **92**, 221503 (2008).
[24]W. M. Posadowski and A. Brudnik, "Optical emission spectroscopy of self-sustained magnetron sputtering," Vacuum **53**, 11 (1999).
[25]M. Hala, N. Viau, O. Zabeida, J. E. Klemberg-Sapieha, and L. Martinu, "Dynamics of reactive high-power impulse magnetron sputtering discharge studied by time- and space-resolved optical emission spectroscopy and fast imaging," J. Appl. Phys. **107**, 043305 (2010).
[26]A. Palmero, H. Rudolph, and F. Habraken, "Study of the gas rarefaction phenomenon in a magnetron sputtering system," Thin Solid Films **515**, 631 (2006).
[27]C. Huo, D. Lundin, M. A. Raadu, A. Anders, J. T. Gudmundsson, and N. Brenning, "On sheath energization and Ohmic heating in sputtering magnetrons," Plasma Sources Sci. Technol. **22**, 045005 (2013).
[28]M. A. Raadu, I. Axnäs, J. T. Gudmundsson, C. Huo, and N. Brenning, "An ionization region model for high-power impulse magnetron sputtering discharges," Plasma Sources Sci. Technol. **20**, 065007 (2011).
[29]C. Huo, D. Lundin, M. A. Raadu, A. Anders, J. T. Gudmundsson, and N. Brenning, "On the road to self-sputtering in high power impulse magnetron sputtering: Particle balance and discharge characteristics," Plasma Sources Sci. Technol. **23**, 025017 (2014).
[30]N. Brenning, J. T. Gudmundsson, D. Lundin, T. Minea, M. A. Raadu, and U. Helmersson, "The role of Ohmic heating in dc magnetron sputtering," Plasma Sources Sci. Technol. **25**, 065024 (2016).
[31]D. Lundin, J. T. Gudmundsson, N. Brenning, M. A. Raadu, and T. M. Minea, "A study of the oxygen dynamics in a reactive Ar/O_2 high power impulse magnetron sputtering discharge using an ionization region model," J. Appl. Phys. **121**, 171917 (2017).
[32]A. Anders, "Localized heating of electrons in ionization zones: Going beyond the Penning-Thornton paradigm in magnetron sputtering," Appl. Phys. Lett. **105**, 244104 (2014).
[33]A. Anders, M. Panjan, R. Franz, J. Andersson, and P. Ni, "Drifting potential humps in ionization zones: The 'propeller blades' of high power impulse magnetron sputtering," Appl. Phys. Lett. **103**, 144103 (2013).
[34]M. Panjan and A. Anders, "Plasma potential of a moving ionization zone in DC magnetron sputtering," J. Appl. Phys. **121**, 063302 (2017).
[35]A. Anders, "Self-organization and self-limitation in high power impulse magnetron sputtering," Appl. Phys. Lett. **100**, 224104 (2012).
[36]P. A. Ni, C. Hornschuch, M. Panjan, and A. Anders, "Plasma flares in high power impulse magnetron sputtering," Appl. Phys. Lett. **101**, 224102 (2012).
[37]A. Hecimovic, "Anomalous cross-B field transport and spokes in HiPIMS plasma," J. Phys. D: Appl. Phys. **49**, 18LT01 (2016).
[38]W. Breilmann, A. Eitrich, C. Maszl, A. Hecimovic, V. Layes, J. Benedikt, and A. v. Keudell, "High power impulse sputtering of chromium: Correlation between the energy distribution of chromium ions and spoke formation," J. Phys. D: Appl. Phys. **48**, 295202 (2015).
[39]A. P. Ehiasarian, J. Andersson, and A. Anders, "Distance-dependent plasma composition and ion energy in high power impulse magnetron sputtering," J. Phys. D: Appl. Phys. **43**, 275204 (2010).
[40]G. Greczynski and L. Hultman, "Time and energy resolved ion mass spectroscopy studies of the ion flux during high power pulsed magnetron sputtering of Cr in Ar and Ar/N_2 atmospheres," Vacuum **84**, 1159 (2010).
[41]A. Hecimovic and A. P. Ehiasarian, "Spatial and temporal evolution of ion energies in high power impulse magnetron sputtering plasma discharge," J. Appl. Phys. **108**, 063301 (2010).
[42]P. Poolcharuansin and J. W. Bradley, "The evolution of the IEDFs in a low-pressure HiPIMS discharge," Surf. Coat. Technol. **205**(2), S307 (2011).
[43]Y. Yang, X. Zhou, J. X. Liu, and A. Anders, "Evidence for breathing modes in direct current, pulsed, and high power impulse magnetron sputtering plasmas," Appl. Phys. Lett. **108**, 034101 (2016).
[44]S. G. Walton, R. F. Fernsler, and D. Leonhardt, "Measurement of ion energy distributions using a combined energy and mass analyzer," Rev. Sci. Instrum. **78**, 083503 (2007).